45.0 ADDITIVE MANUFACTURING FEASIBILITY OF REFRACTORY ALLOYS

Abby Miklas (Mines)
Faculty: Amy Clarke, Jonah Klemm-Toole (Mines)
Industrial Mentor: Andy Deal (Kansas City National Security Campus), Andrew Kustas (Sandia National Laboratories), Noah Phillips (ATI)

This project initiated in Fall 2020 and is supported by Kansas City National Security Campus. The research performed during this project will serve as the basis for a MS thesis program for Abby Miklas.

45.1 Project Overview and Industrial Relevance

Alloys have historically been based on a single principal element or constituent. However, by limiting the composition to only one principal component, the possible microstructures and properties are also limited [45.1]. High entropy alloys (HEAs) present an opportunity to expand the useable area of the phase diagram and make new composition spaces possible. They offer unique property combinations that exceed those of conventional alloys, for instance high strength without deficits in ductility [45.2]. One specific area that conventional alloys, specifically Ni or Co based superalloys, have traditionally dominated is high temperature applications. Refractory HEAs (RHEAs) offer the unique properties characteristic of HEAs, as well as ultra-high temperature capabilities that allow them to operate in extreme environments and exceed the performance of existing Ni and Co based superalloys. While RHEAs have the potential to expand the temperature capabilities of superalloys, they are not widely used because they are difficult to manufacture through conventional methods [45.3]. RHEAs are traditionally manufactured by casting, but because they can maintain their high strength at ultra-high temperatures, RHEAs are not only difficult to fabricate with conventional forming and machining techniques but also difficult to thermomechanically process to achieve desired microstructures [45.4]. Therefore, opportunity exists to develop production methods that would enable RHEAs to be used more readily in ultra-high temperature applications. Additive manufacturing (AM) is capable of producing near-net shape parts with tailored microstructures. AM process parameters are easily manipulated to affect the melt pool and produce the desired microstructures [45.5].

In this project, four refractory alloys, including two refractory binaries (Mo30Nb and Nb7.5Ta) and two RHEAs (C103 and MoNbTaTi), are each subjected to five single track laser track welds that use different parameters to vary the melt pool morphology. These welds will be evaluated metallographically via scanning electron microscopy (SEM), electron backscatter diffraction (EBSD), and x-ray diffraction (XRD) to understand the solidification and microstructure development that occurs in the refractory alloys when subjected to additive manufacturing conditions. Thermal gradient modeling will be completed for the laser track welds with SYSWELD and columnar to equiaxed transition (CET) modeling will be completed using data generated with thermodynamic modeling. These models will then be compared to the microstructure characterization results. Ultimately, this work seeks to create strategies for microstructure development by additive manufacturing to achieve tailored microstructures that will enable RHEAs to be more widely used in ultra-high temperature applications.

45.2 Previous Work (Work that was done since the beginning of the project, or literature review)

45.2.1 Solidification Simulations

Scheil solidification simulations were completed in Themo-Calc using the HEAs database package, which includes TCHEA4 and MOBHEA2. Simulations were complete for each alloy of interest. It is predicted that in the Mo30Nb that the first solid to form will be depleted in Nb at less than 70 mole percent, while it will be rich in Mo at more than 30 mole percent. The last solid to form is conversely rich in Nb and depleted in Mo. The Nb7.5Ta displays a similar trend where the Nb is depleted in the first solid to form and rich in the last. The Ta is correspondingly rich in the first solid to form and depleted in the last. For C103, the four elements with the largest mole percent contribution

were selected to be included in the simulation. Unlike in the other alloys, the Nb in the C103 is predicted to be rich in the first solid to form and depleted in the last. The Hf, Zr, and Ti all behave as expected; it is predicted that the fist solid to form will be depleted in these elements, while the last to form with be rich in them. Finally, in the MoNbTaTi, it was found that Nb and Ti are both depleted in the first solid to form and rich in the last solid to form, while Mo and Ta are both rich in the first solid to form and depleted in the last.

45.2.2 Solid Solution Strengthening Evaluation

Vickers hardness measurements were taken on a LECO AMH55 Automated Hardness Indenter for five Mo and Nb binary alloys of various compositions. The LECO AMH55 Automated Hardness Indenter is calibrated according to ASTM E92 and performs microhardness indentation in accordance with ASTM E384. The compositions tested were Mo10Nb, Mo30Nb, Nb50Mo, Nb30Mo, and Nb10Mo. All samples were in the as-cast condition except for Nb10Mo, which had been rolled. Each sample was mounted in Bakelite, then ground and polished to 1 μm prior to testing. 20 microindentations were performed on each sample using a force of 200 gf in a straight-line indentation pattern with a 150 μm spacing between indentations. The force was selected to ensure the indent size was not so large that it did not comply with ASTM E384 depth requirements, but not so small that more scatter was introduced to the data [45.9]. The spacing was selected to comply with ASTM E384 guidelines. The measured Vickers hardness was observed to generally increase with increasing alloying additions. The solid solution strengthening behavior was described using fit models.

45.3 Recent Progress

45.3.1 Single-Track Laser Melts

Samples measuring approximately 1/2" x 1/2" x 3/8" were sectioned from bulk material of each of the alloys of interest. Each sample was ground to be flat and parallel. The finished surface was ground with 1200 grit sandpaper to prepare the surface for the laser track melts. Five laser track melts were performed on each sample. The location of the five melts on each sample is shown in **Figure 45.1**. Different combinations of laser powers and speeds were used for each of the five melts. The parameters used for each track are detailed in **Table 45.1**.
Low magnification top-down imaging has been completed to characterize the weld behavior. Images are included in **Figure 45.2**. The two Mo-containing alloys exhibited surface cracking in all five laser track melts that was more severe than in the other alloys. All alloys exhibited balling for parameter set four, which corresponds to the highest power and speed used. The Nb7.5Ta, C103, and MoNbTaTi exhibited balling for parameter set five as well while the Mo30Nb did not. Parameter set five corresponds to the second highest power and the highest speed used.

45.3.2 Solidification Modeling

Alloy-specific solidification maps, shown in **Figure 45.3**, were created for each alloy of interest so that the microstructure of the final laser melted sample can be predicted. A combination of experimental solidification velocities and modeled thermal gradients can be used to predict whether a given process and alloy combination will produce a fully columnar, fully equiaxed, or mixed microstructure. The CET models presented were based on a simplified Kurz-Giovanola-Trivedi (KGT) model [45.6]. In this simplified model, solute diffusivities D_i, partitioning coefficients k_i, and liquidus slopes m_i were assumed to be constant. The Gibbs-Thomson coefficient Γ and the solute diffusivities were taken from literature while the partitioning coefficients and liquidus slopes were modeled in Thermo-Calc using the TCHEA5 database. The initial solute concentration C_i, is known from the alloy composition. The model also utilizes the Peclet number P_i, the solidification thermal gradient G, the tip radius R, and the solidification velocity V. The input parameter values used for each alloy are depicted in **Table 45.2**. The equations used for this model are described in **Equations 45.1 – 45.7**. **Equations 45.1** and **45.2** are used in **Equations 45.3** and **45.4** to calculate R and V. **Equations 45.5**, **45.6**, and **45.7** are used to calculate the solute undercooling, the curvature, and the total undercooling, respectively.

45.2

$$\xi_i = 1 - \frac{2k_i}{\sqrt{1 + \left(\frac{2\pi}{P_i}\right)^2} - 1 + 2k_i} \tag{45.1}$$

$$C_i^* = \frac{C_o}{1 - [(1 - k_i)lv(P_i)]} \tag{45.2}$$

$$4\pi^2\Gamma\left(\frac{1}{R^2}\right) + \left(2\sum[m_iP_i(1 - k_i)C_i^*\xi_i]\right)\left(\frac{1}{R}\right) + G = 0 \tag{45.3}$$

$$V = \frac{2P_iD_i}{R} \tag{45.4}$$

$$\Delta T_{c,i} = m_i(C_o - C_i^*) \tag{45.5}$$

$$\Delta T_r = \frac{2\Gamma}{R} \tag{45.6}$$

$$\Delta T_{total} = \sum_i \Delta T_{c,i} + \Delta T_r \tag{45.7}$$

Before creating the solidification maps, the undercooling plots for each alloy shown in **Figure 45.6** were created using the above equations. The undercooling plots show both total undercooling for the alloy as well as undercooling for each individual constituent. This can be useful in guiding future alloy compositions. These plots also show that the predicted absolute stability velocities for the alloys range from approximately 1.0E-2 to 1.0 m/s, which is slower than anticipated. This predicted range is expected to change as further information from the microstructure evaluation and thermal gradient modeling is used to refine the model.

The total undercooling in **Figure 45.6** is fit with a power law model, **Equation 45.8**, to determine the material constants a and n in. These are then used in **Equation 45.9** to compute G and complete the CET models shown in **Figure 45.3**. In **Equation 45.9**, N_o is the nucleation site density, Φ is the volume fraction of equiaxed grains, and ΔT_n is the nucleation undercooling [45.7].

$$\Delta T = (a * V)^{1/n} \tag{45.8}$$

$$G = \frac{1}{n+1} * \left(\frac{-4\pi N_o}{3\ln(1 - \Phi)}\right)^{\frac{1}{3}} * \left(1 - \frac{\Delta T_n^{n+1}}{(A * V)^{\frac{n}{n+1}}}\right) * (A * V)^{\frac{1}{n}} \tag{45.9}$$

A comparison of the 50% equiaxed plots for each alloy is shown in **Figure 45.4**. This shows that C103 is predicted to exhibit the highest amount of equiaxed grains. **Figure 45.5** shows the 50% equiaxed line for MoNbTaTi plotted four ways with each of the primary constituents assumed to be the "base" element. Because the MoNbTaTi is equiatomic, there is not a clear path for defining the "base" element and solute elements. The plots for MoNbTaTi depicted in **Figures 45.3** and **45.4** show a scenario where the highest melting temperature element Ta, was assumed to be the "base" element. However, **Figure 45.5** shows that assuming the element with the largest contribution to total undercooling Nb, was the "base" element produces similar results and even predicts a higher quantity of equiaxed grains.

45.3.3   Thermal Gradient Modeling

The conduction-only program SYSWELD is being used perform simple models of the single-track melts. The density, thermal conductivity, and specific heat for each alloy were modeled as a function of temperature in Thermo-Calc using the TCHEA5 database. A mesh has been established for each material and each laser track melt parameter. Preliminary simulations have been completed.

45.3

45.4   Plans for Next Reporting Period

- High magnification top-down imaging of the laser track melts will be completed.
- CET/solidification modeling will be completed.
- Thermal gradient modeling in SYSWELD will be completed.
- Microstructure characterization of the melt tracks using SEM, EBSD, and XRD will be completed.
- Thesis writing will have begun.

45.5   References

[45.1]   B. S. Murty, J. W. Yeh, and S. Ranganathan, "Chapter 2 - High-Entropy Alloys: Basic Concepts," in High entropy alloys, Butterworth-Heinemann, 2014.

[45.2]   Y. F. Ye, Q. Wang, J. Lu, C. T. Liu, and Y. Yang, "High-entropy alloy: Challenges and prospects," *Materials Today*, vol. 19, no. 6, pp. 349–362, 2016.

[45.3]   N. R. Philips, M. Carl, and N. J. Cunningham, "New opportunities in refractory alloys," *Metallurgical and Materials Transactions*, vol. 51, no. 7, pp. 3299–3310, 2020.

[45.4]   Y. Zhang and Q. Xing, "High entropy alloys: Manufacturing Routes," *Encyclopedia of Materials: Metals and Alloys*, pp. 327–338, 2022.

[45.5]   Torralba, J. M., Campos, M. (2020). High Entropy Alloys Manufactured by Additive Manufacturing. Metals, 10(5), 639. doi:10.3390/met10050639.

[45.6]   W. Kurz, B. Giovanola, and R. Trivedi, "Theory of microstructural development during Rapid Solidification," *Acta Metallurgica*, vol. 34, no. 5, pp. 823–830, 1986.

[45.7]   M. Gäumann, C. Bezençon, P. Canalis, and W. Kurz, "Single-crystal laser deposition of superalloys: Processing–microstructure maps," Acta Materialia, vol. 49, no. 6, pp. 1051–1062, 2001.

[45.8]   M. Haines, A. Plotkowski, C. L. Frederick, E. J. Schwalbach, and S. S. Babu, "A sensitivity analysis of the columnar-to-equiaxed transition for ni-based superalloys in electron beam additive manufacturing," *Computational Materials Science*, vol. 155, pp. 340–349, 2018.

[45.9]   M. R. Rolchigo and R. LeSar, "Modeling of binary alloy solidification under conditions representative of Additive Manufacturing," *Computational Materials Science*, vol. 150, pp. 535–545, 2018.
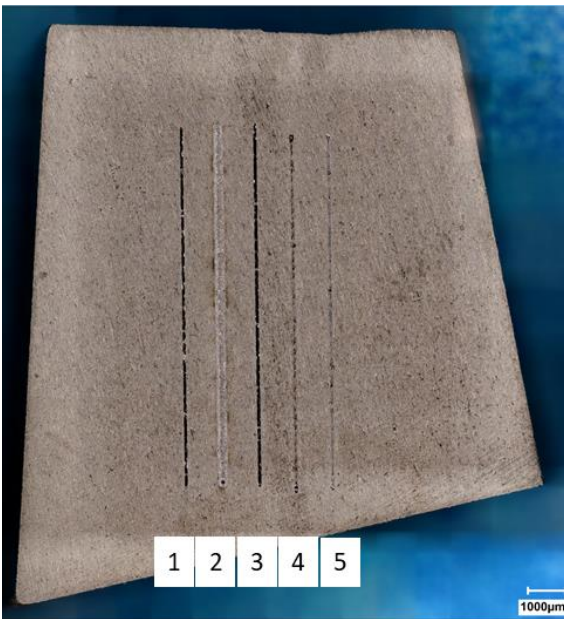
45.6   **Figures and Tables**
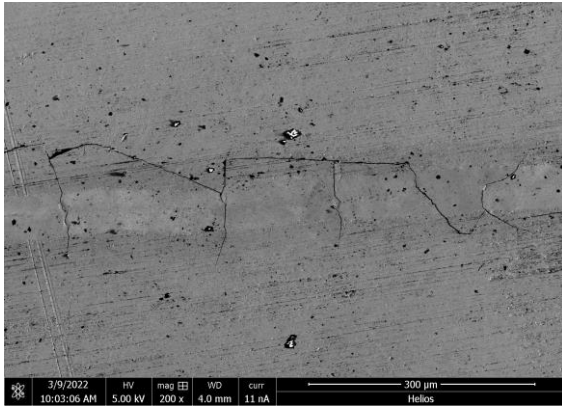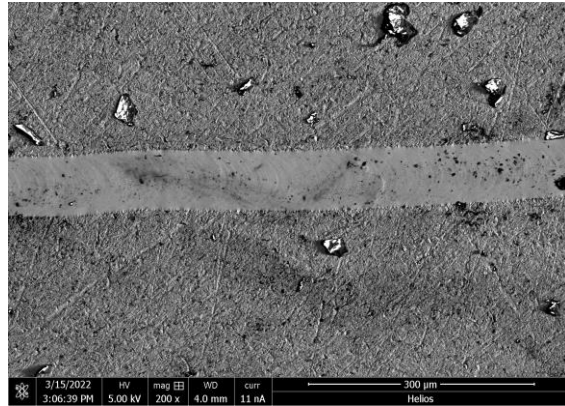

(a)
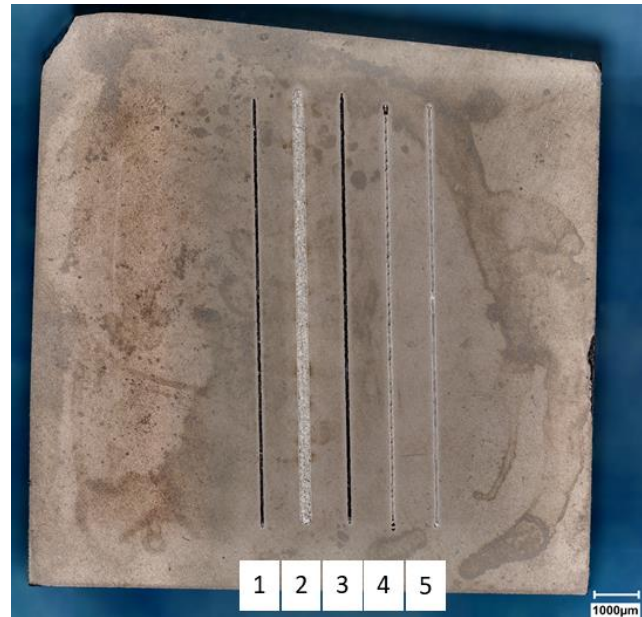
(b)

(c)

(d)

Figure 45.1: Top-down macro images of the five melt tracks completed on samples of Mo30Nb (a), Nb7.5 Ta (b), C103 (c), and MoNbTaTi (d). Each weld is labelled 1-5 which correlates to parameters detailed in Table 45.1. Images were taken on a Keyence VHX-5000.
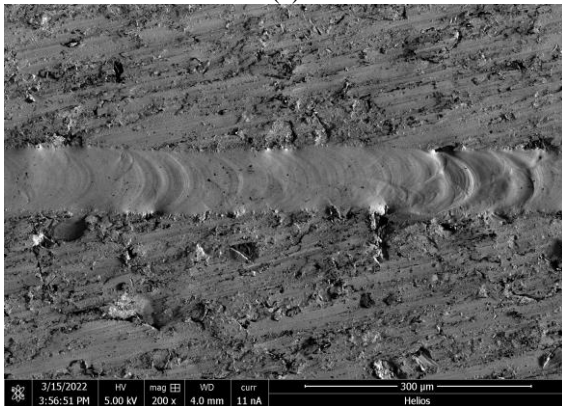
45.5
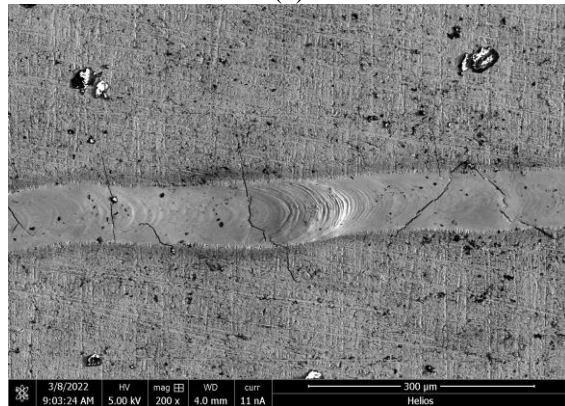
(a)

(b)

(c)

(d)

(e)

(f)

45.6

(g)

(h)

(i)

(j)

(k)

(l)

45.7

(m)

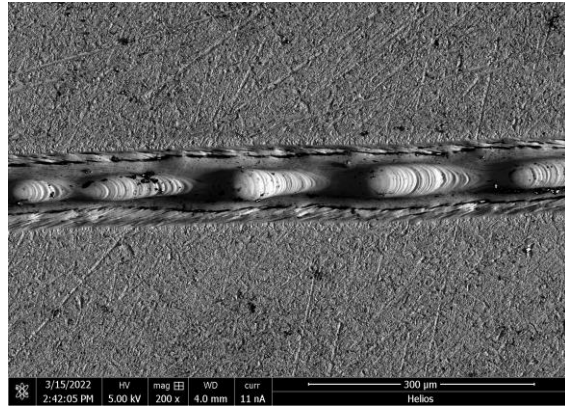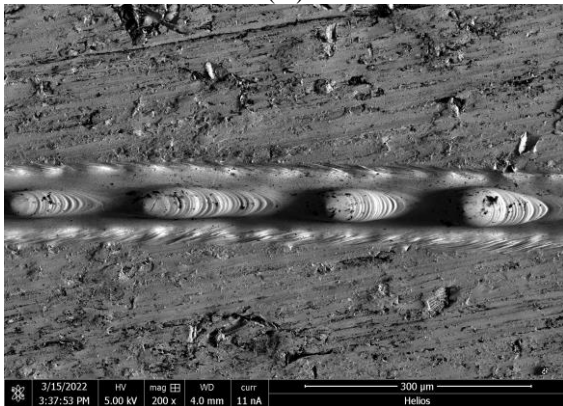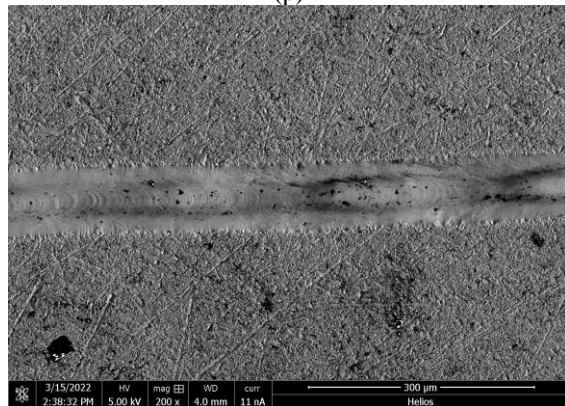(n)

(o)

(p)

(q)

(r)

45.8

(s)

(t)
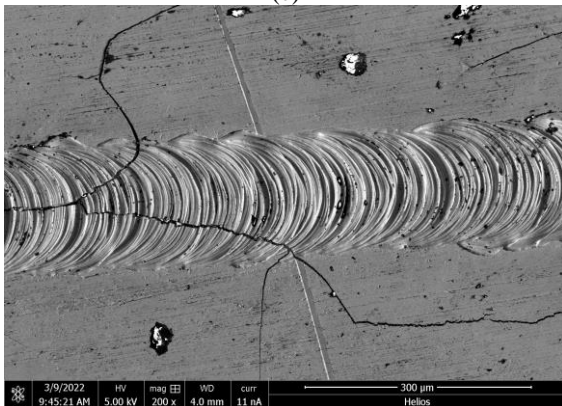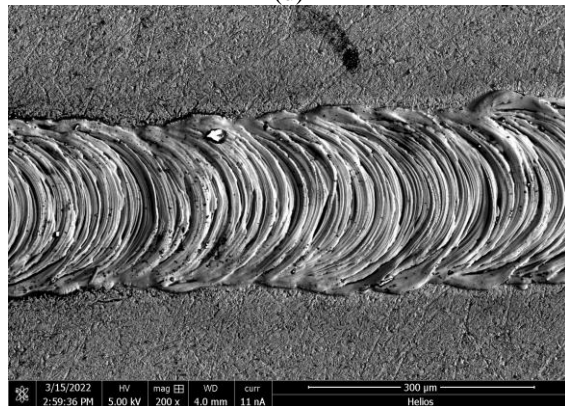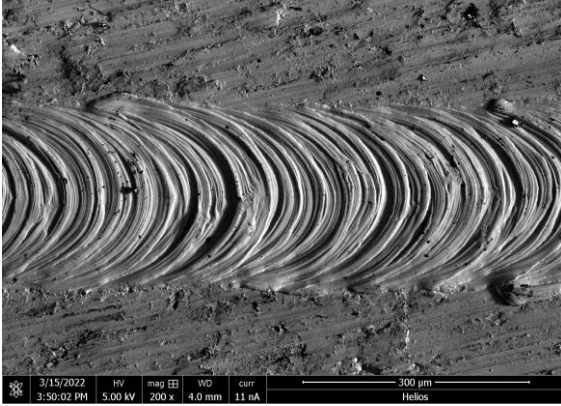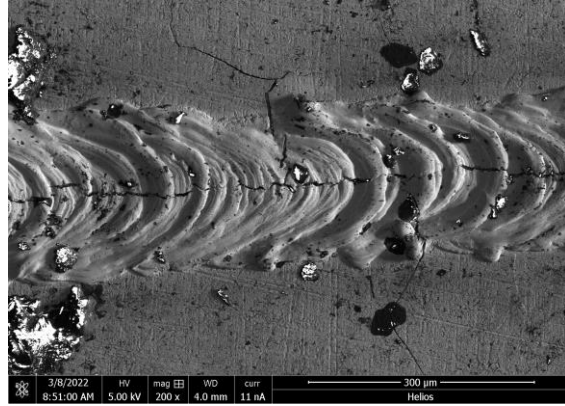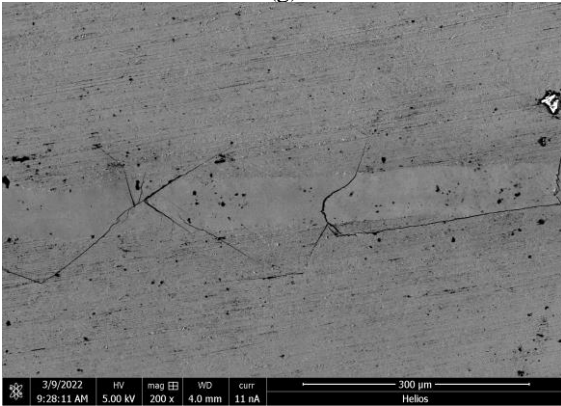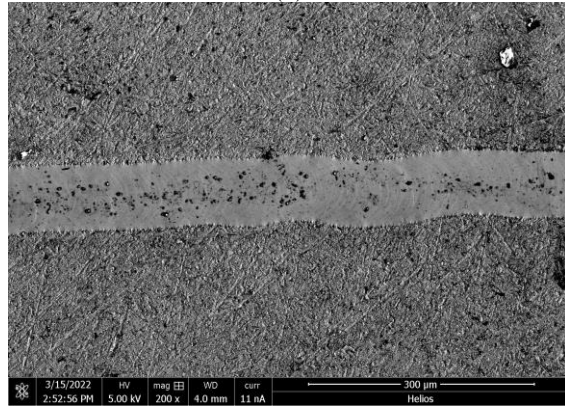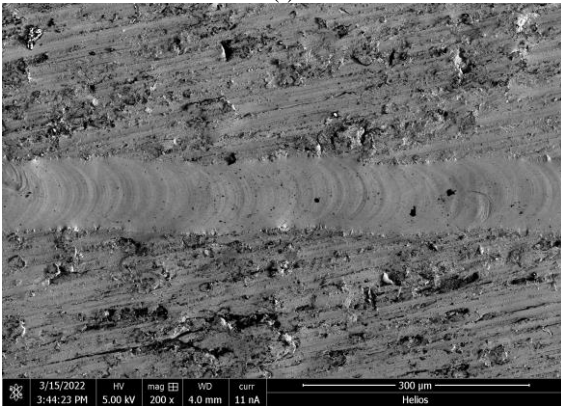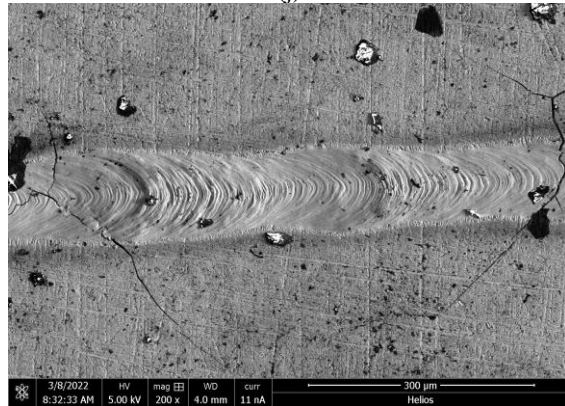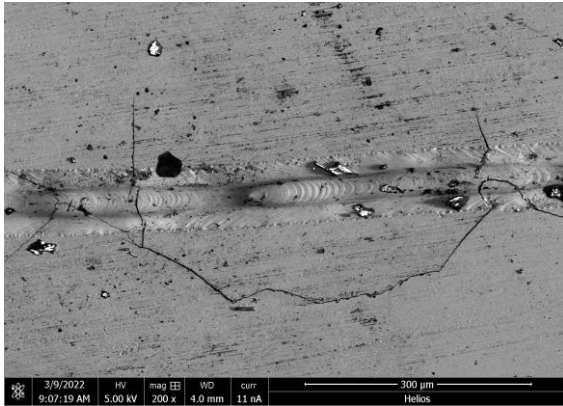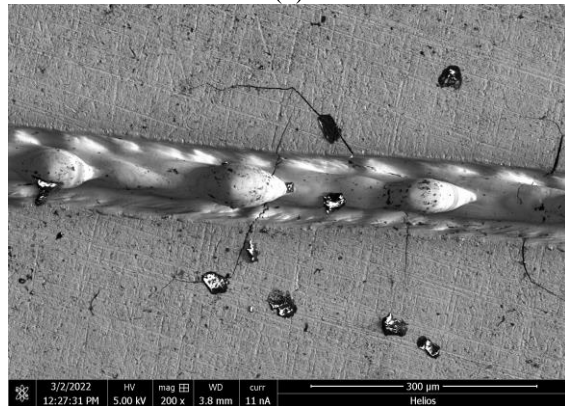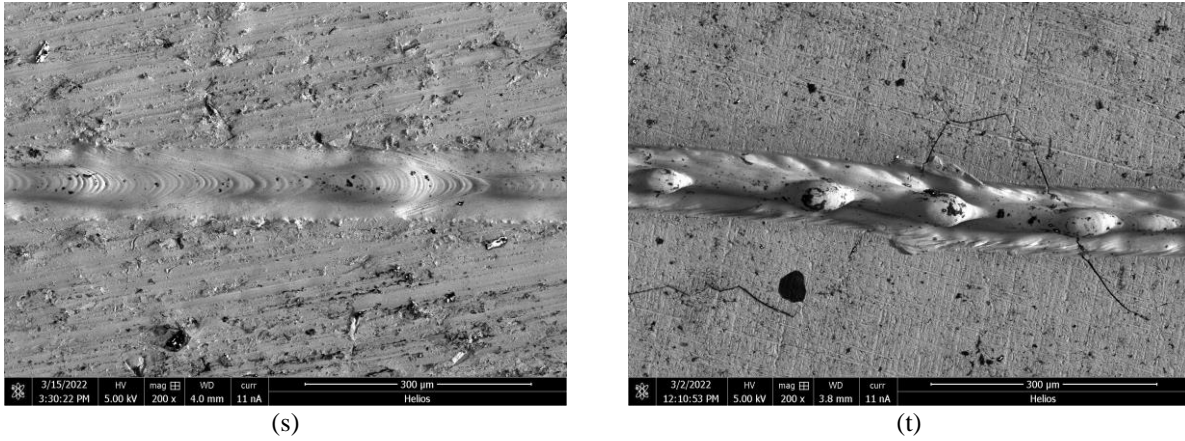
Figure 45.2: Low magnification top-down images of each laser track melt parameter set on all four materials. Images (a) – (d) show parameter set one on Mo30Nb (a), Nb7.5 Ta (b), C103 (c), and MoNbTaTi (d). Images (e) – (h) show parameter set two on Mo30Nb (e), Nb7.5 Ta (f), C103 (g), and MoNbTaTi (h). Images (i) – (l) show parameter set three on Mo30Nb (i), Nb7.5 Ta (j), C103 (k), and MoNbTaTi (l). Images (m) – (p) show parameter set four on Mo30Nb (m), Nb7.5 Ta (n), C103 (o), and MoNbTaTi (p). Images (q) – (t) show parameter set one on Mo30Nb (q), Nb7.5 Ta (r), C103 (s), and MoNbTaTi (t).

(a)

(b)

45.9
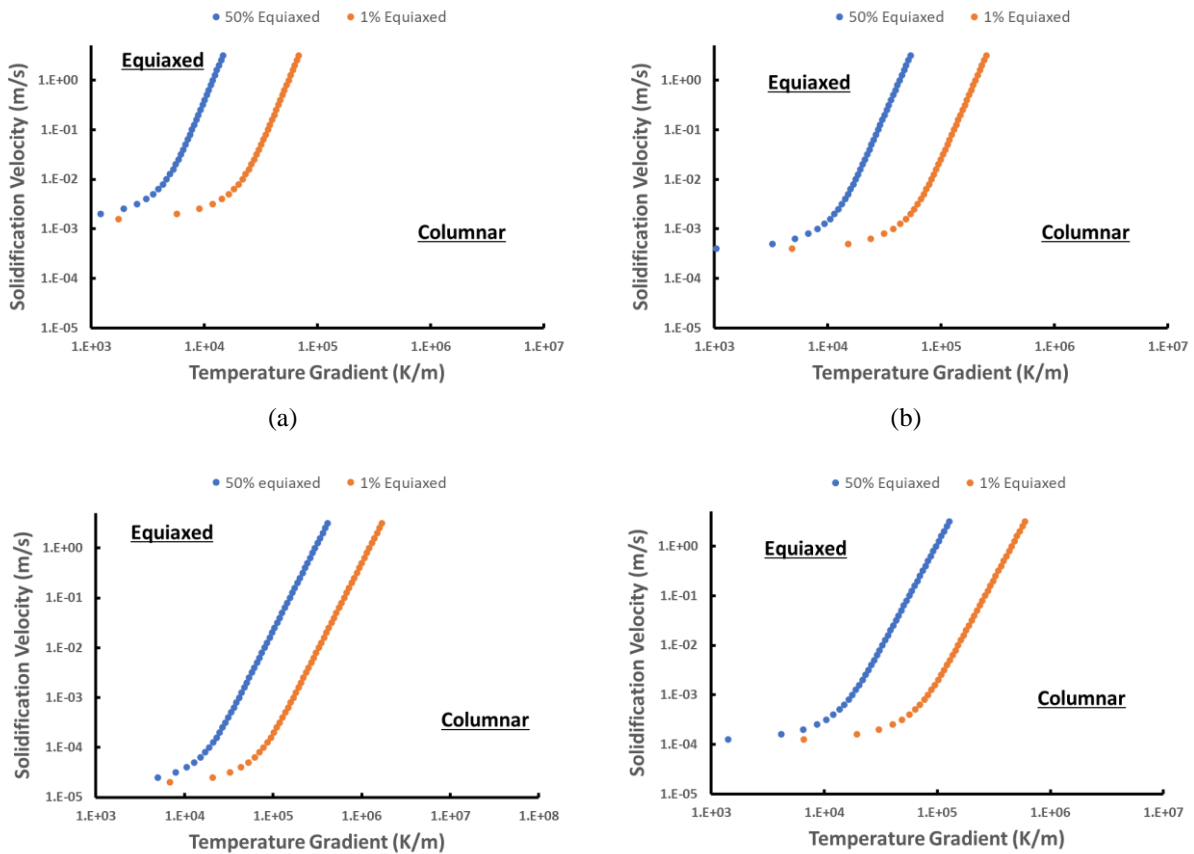
(c)   (d)

Figure 45.3: CET solidification maps for Mo30Nb (a), Nb7.5 Ta (b), C103 (c), and MoNbTaTi (d).

Figure 45.4: CET solidification map comparing the 50% equiaxed plots for all four alloys.
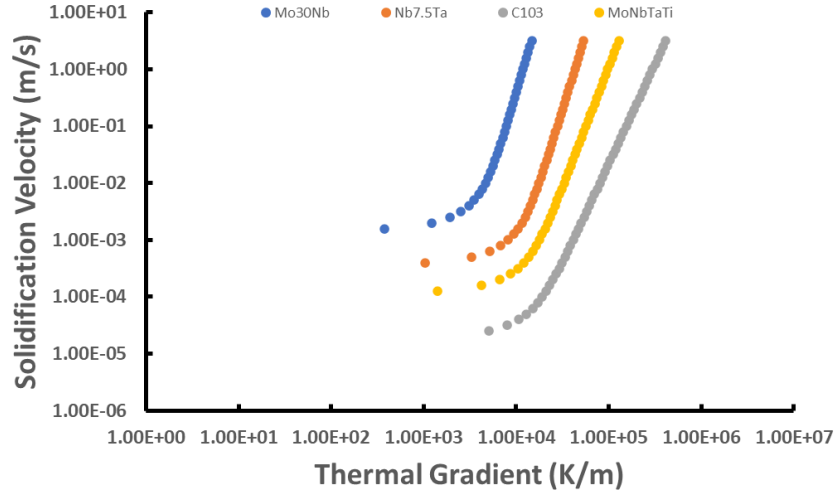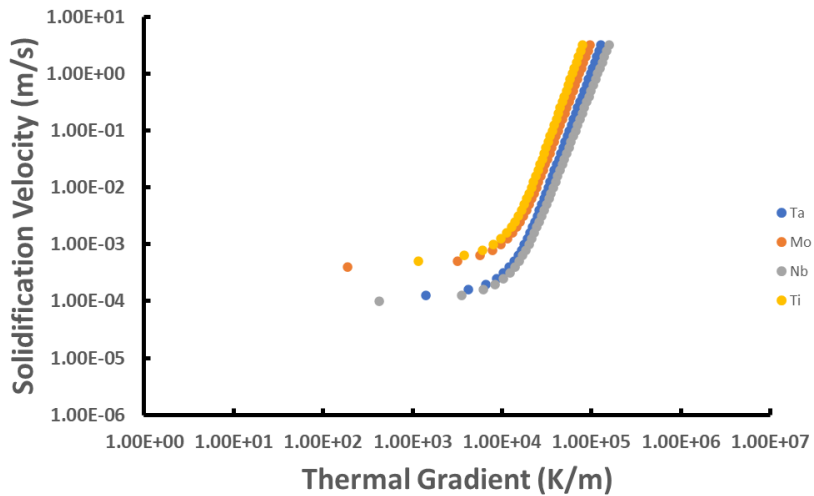

Figure 45.5: CET solidification map comparing the 50% equiaxed plots for MoNbTaTi assuming each of the primary constituents as the "base" element.

45.10

(a)

(b)

(c)

(d)
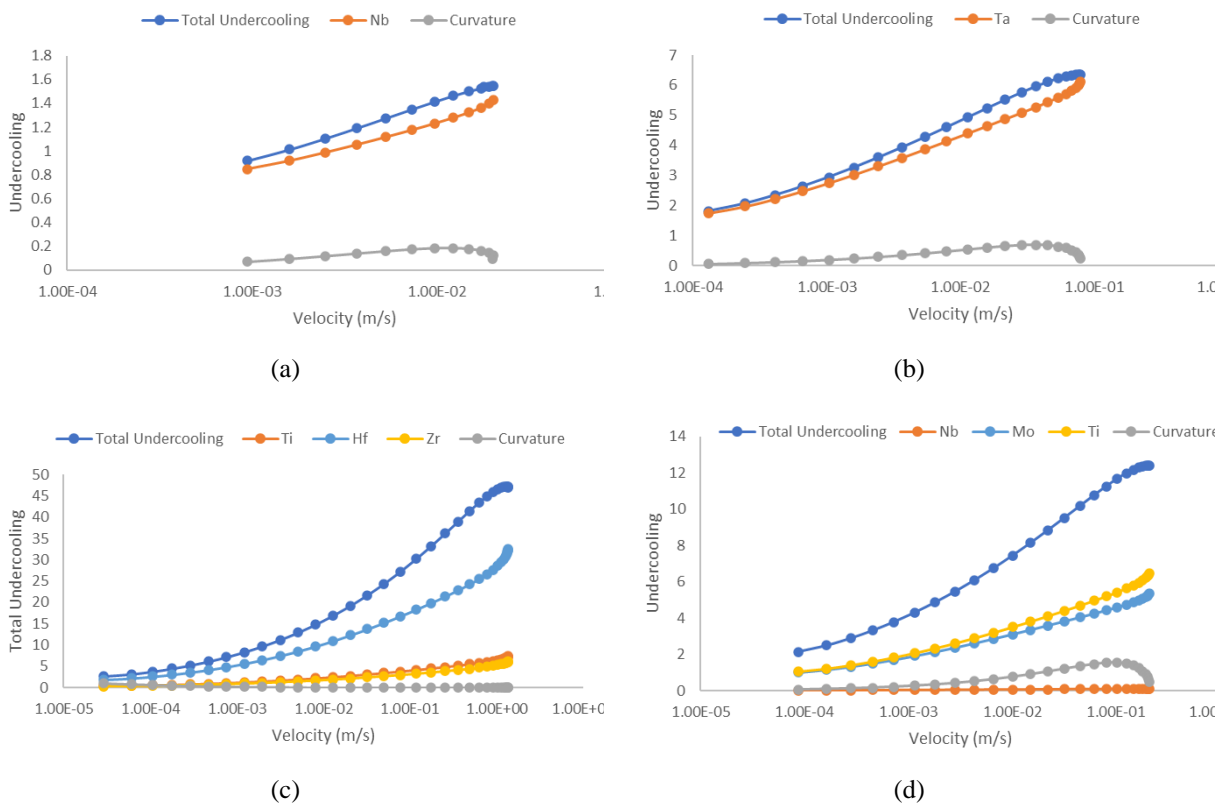
Figure 45.6: Total undercooling, undercooling contribution of each solute, and curvature predictions for Mo30Nb (a), Nb7.5 Ta (b), C103 (c), and MoNbTaTi (d).

Table 45.1: Laser parameters used for each weld number on all samples depicted in Figure 45.1.

Parameter Set	Power [W]	Speed [m/s]
1	162	0.8
2	243	0.2
3	162	0.5
4	405	1.7
5	324	1.7

Table 45.2: CET parameters for each alloy with all "base" element possibilities for MoNbTaTi depicted.

Alloy	"Base" Element	Solute	Parameter	Value
Mo30Nb	Mo		Gibbs-Thomson Coefficient [45.8]	1.92E-7 K*m
		Nb	Diffusion Coefficient [45.9]	2.00E-9 m^2/s
			Partition Coefficient	0.97

45.11

Alloy	Solvent	Solute	Property	Value
			Liquidus Slope	-1.45 K/wt.%
			Initial Concentration	30.0 wt.%
Nb7.5Ta	Nb	Ta	Gibbs-Thomson Coefficient [45.8]	1.92E-7 K*m
			Diffusion Coefficient [45.9]	2.00E-9 m^2/s
			Partition Coefficient	1.26
			Liquidus Slope	4.08 K/wt.%
			Initial Concentration	7.5 wt.%
C103	Nb	Hf	Gibbs-Thomson Coefficient [45.8]	1.92E-7 K*m
			Diffusion Coefficient [45.9]	2.00E-9 m^2/s
			Partition Coefficient	0.57
			Liquidus Slope	-4.93 K/wt.%
			Initial Concentration	9.0 wt.%
		Zr	Diffusion Coefficient [45.9]	2.00E-9 m^2/s
			Partition Coefficient	0.51
			Liquidus Slope	-9.34 K/wt.%
			Initial Concentration	0.7 wt.%
		Ti	Diffusion Coefficient [45.9]	2.00E-9 m^2/s
			Partition Coefficient	0.58
			Liquidus Slope	-14.91 K/wt.%
			Initial Concentration	0.7 wt.%
MoNbTaTi	Ta	Mo	Gibbs-Thomson Coefficient [45.8]	1.92E-7 K*m
			Diffusion Coefficient [45.9]	2.00E-9 m^2/s
			Partition Coefficient	1.04
			Liquidus Slope	6.03 K/wt.%
			Initial Concentration	23.0 wt.%
		Nb	Diffusion Coefficient [45.9]	2.00E-9 m^2/s
			Partition Coefficient	0.95
			Liquidus Slope	-0.09 K/wt.%
			Initial Concentration	22.2 wt.%
		Ti	Diffusion Coefficient [45.9]	2.00E-9 m^2/s
			Partition Coefficient	0.88
			Liquidus Slope	-4.45 K/wt.%
			Initial Concentration	11.5 wt.%
MoNbTaTi	Mo	Nb	Gibbs-Thomson Coefficient [45.8]	1.92E-7 K*m
			Diffusion Coefficient [45.9]	2.00E-9 m^2/s
			Partition Coefficient	0.95
			Liquidus Slope	-0.09 K/wt.%
			Initial Concentration	22.2 wt.%
		Ta	Diffusion Coefficient [45.9]	2.00E-9 m^2/s
			Partition Coefficient	1.04
			Liquidus Slope	1.14 K/wt.%
			Initial Concentration	43.3 wt.%
		Ti	Diffusion Coefficient [45.9]	2.00E-9 m^2/s
			Partition Coefficient	0.88
			Liquidus Slope	-4.45 K/wt.%
			Initial Concentration	11.5 wt.%
MoNbTaTi	Nb	Mo	Gibbs-Thomson Coefficient [45.8]	1.92E-7 K*m
			Diffusion Coefficient [45.9]	2.00E-9 m^2/s
			Partition Coefficient	1.04

45.12

			Liquidus Slope	6.03 K/wt.%
			Initial Concentration	23.0 wt.%
		Ta	Diffusion Coefficient [45.9]	2.00E-9 m^2/s
			Partition Coefficient	1.04
			Liquidus Slope	1.14 K/wt.%
			Initial Concentration	43.3 wt.%
		Ti	Diffusion Coefficient [45.9]	2.00E-9 m^2/s
			Partition Coefficient	0.88
			Liquidus Slope	-4.45 K/wt.%
			Initial Concentration	11.5 wt.%
MoNbTaTi	Ti		Gibbs-Thomson Coefficient [4587]	1.92E-7 K*m
		Mo	Diffusion Coefficient [45.9]	2.00E-9 m^2/s
			Partition Coefficient	1.04
			Liquidus Slope	6.03 K/wt.%
			Initial Concentration	23.0 wt.%
		Nb	Diffusion Coefficient [45.9]	2.00E-9 m^2/s
			Partition Coefficient	1.04
			Liquidus Slope	1.14 K/wt.%
			Initial Concentration	43.3 wt.%
		Ta	Diffusion Coefficient [45.9]	2.00E-9 m^2/s
			Partition Coefficient	0.95
			Liquidus Slope	-0.09 K/wt.%
			Initial Concentration	22.2 wt.%

45.13